Energy Conversion and Management 365 (2026) 121743

Contents lists available at ScienceDirect

Energy Conversion and Management

journal homepage: www.elsevier.com/locate/enconman

An experimental study on the coupling effect of swirl ratio and injection timing in reactivity-controlled compression ignition gas engines

Jacek Hunicz [a,b], Liping Yang [c], Shuaizhuang Ji [c], Maciej Mikulski [b,*]

[a] Faculty of Mechanical Engineering, Lublin University of Technology, Lublin 20-618, Poland
[b] Efficient Powertrain Solutions (EPS), School of Technology and Innovations, University of Vaasa, Vaasa FI-65200, Finland
[c] College of Power and Energy Engineering, Harbin Engineering University, Harbin 150001, China

ARTICLE INFO

Keywords:
RCCI
Natural gas
In-cylinder flow
Swirl ratio
Start of injection
Emissions

ABSTRACT

This study investigates the coupled effects of swirl ratio and start of injection on diesel–natural gas reactivity-controlled compression ignition, with particular focus on their unexplored interactions and their effects on combustion characteristics and emissions. Experiments were conducted on a single-cylinder research engine at a representative operating point, using four distinct intake port configurations to generate swirl. Diesel injection timing was swept between 34 and 47 crank angle degrees before top dead centre, constrained by misfire limits. In-cylinder pressure-based thermodynamic analysis, along with flow simulations, enabled the interpretation of how in-cylinder turbulence influences combustion. The results for the first time reveal that swirl has a limited effect on cylinder-bowl-initiated ignition but plays a dominant role in combustion development as it progresses into the squish region. A high swirl advanced combustion phasing by 5.4 degrees and increased the peak heat release rate by 20%, but reduced combustion efficiency by up to four percentage points compared with low-swirl configurations. This was attributed to excessive homogenisation of the mixture and greater wall heat losses, which also increased unburnt hydrocarbon and carbon monoxide emissions. Nitrogen oxides emissions correlated strongly with combustion timing and temperature, while remaining largely insensitive to swirl. There was no direct trade-off between nitrogen oxides and particulate emissions, with particulate mass remaining ultra-low. However, more premixed conditions (early injection and large swirl) produced more fine particles, with particulate number emissions double the EU Stage V limit. The neutral-port-only configuration, combining the lowest swirl with the highest average turbulent kinetic energy, yielded optimal performance, with the highest thermal efficiency, nearly 44%, and the lowest combined carbon monoxide and hydrocarbon emissions. The results demonstrate that reactivity-controlled compression ignition performance is governed by a balance between swirl- and tumble-driven flow structures rather than by swirl intensity alone, and that flow-injection optimisation can enable compliance with stringent off-road emission limits without exhaust aftertreatment.

1. Introduction

Reactivity-controlled compression ignition (RCCI) is an extension of premixed charge compression ignition, a combustion concept utilising two fuels with different auto-ignition properties [1]. Its core principle is using fuel injection strategies and intake charge management to control in-cylinder fuel reactivity stratification. This approach provides a well-mixed air–fuel charge while enabling precise control of combustion phasing, thereby improving engine efficiency and reducing emissions.

A typical RCCI engine utilises a diesel engine platform, with direct injection of a high-reactivity fuel (HRF) and port fuel injection of a low-reactivity fuel (LRF) [2]. The selection and interaction of LRF and HRF are central to the concept performance, directly influencing combustion efficiency, emissions and operating range. Low-reactivity fuels such as gasoline, natural gas or alcohols promote premixed combustion and reduce nitrogen oxides (NO_X) and soot formation, while high-reactivity fuels such as diesel or biodiesel control ignition timing and combustion phasing.

The mainstream approach to RCCI performance and emission control focuses on optimising controllable engine parameters and tailoring the fuel. Most studies focus on tuning injection strategies for HRF, the blend ratio (energy fraction of premixed LRF), the exhaust gas recirculation (EGR) rate, and boost pressure [3]. The most important achievements in terms of efficiency and emissions, plus application limitations, are summarised below.

* Corresponding author.
E-mail address: maciej.mikulski@uwasa.fi (M. Mikulski).

https://doi.org/10.1016/j.enconman.2026.121743
Received 10 January 2026; Received in revised form 24 May 2026; Accepted 30 May 2026
Available online 5 June 2026

Nomenclature

Acronyms

BDC	bottom dead centre
BMEP	brake mean effective pressure
bTDC	before top dead centre
CA05	crank angle at 5% fuel burnt
CA50	crank angle at 50% fuel burnt
CAD	crank angle degree
CFD	computational fluid dynamics
CoV	coefficient of variation
EGR	exhaust gas recirculation
FTIR	Fourier transform infrared
HRF	high-reactivity fuel
HRR	heat release rate
IMEP	indicated mean effective pressure
ID	ignition delay
ITE	indicated thermal efficiency
LHV	lower heating value
LRF	low-reactivity fuel
NG	natural gas
NMHC	non-methane hydrocarbons
NO_X	nitrogen oxides
PM	particulate matter
PN	particle number
PRR	pressure rise rate
RCCI	reactivity-controlled compression ignition
SOI	start of injection
SR	swirl ratio
TDC	top dead centre
TKE	turbulent kinetic energy
UHC	unburnt hydrocarbons

Extensive experimental investigations by Reitz et al. [4], on a heavy-duty engine fuelled with diesel and gasoline, demonstrated that a gross indicated thermal efficiency (ITE) of up to 56% at an indicated mean effective pressure (IMEP) of approximately 0.93 MPa is attainable. Stable operation over a load range from 0.2 MPa to nearly 1.5 MPa IMEP at an engine speed of 1,300 rpm was demonstrated. Further optimisation of combustion phasing and thermodynamic conditions, including operation at a high compression ratio of 18.7:1 and without piston oil cooling, has indicated the potential to reach gross ITE approaching 60%, providing a pathway towards achieving 50–55% brake thermal efficiency targets. The primary enabler of this improvement was the significant reduction in heat transfer losses compared with conventional diesel combustion. Similarly, Benajes et al. [5] reported a 7% improvement in efficiency (including urea penalty compensation) in diesel-gasoline RCCI compared with conventional diesel, notably at a reduced compression ratio from 17.5:1 to 15.3:1.

In low-displacement engines, indicated thermal efficiency is typically lower; however, RCCI demonstrates consistent performance benefits. For example, Duan et al. [6] achieved 45% net ITE at an IMEP of 0.7 MPa on a 500 cm3 engine with a 16.7:1 compression ratio and gasoline as LRF. Notably, efficiency rose to 47% for the reversed RCCI mode, where HRF was port-injected and LRF stratified via direct injection.

However, the most significant advantage of RCCI lies in its low emissions. Low-temperature, volumetric combustion reduces NO_X emissions, while a homogeneous charge effectively prevents particulate matter (PM) formation. Reitz et al. [4] demonstrated NO_X reductions of nearly three orders of magnitude and approximately sixfold reductions in soot emissions compared with state-of-the-art conventional diesel combustion without EGR. Benajes et al. [5] achieved NO_X and soot emissions below heavy-duty engine Euro VI limits across full speed and load ranges. However, breaking the NO_X-soot trade-off is accompanied by increased emissions of unburned hydrocarbons (UHC) and CO, often by approximately one order of magnitude compared with conventional diesel operation, particularly in light-duty engines, necessitating the use of oxidation catalysts [7].

On the fuel side, various combinations of HRFs and LRFs have been explored, including both fossil-based and renewable alternatives. Natural gas (NG), widely recognised as a transitional decarbonisation fuel, has been thoroughly investigated as LRF. Its high octane number extends the high-load limit but also exacerbates incomplete combustion, reducing efficiency [8]. Furthermore, unburnt methane poses challenges for greenhouse gas emissions and aftertreatment operations [9]. Similarly, alcohol fuels such as E85 improve high-load operability, while oxygenated biodiesels as HRFs enhance combustion efficiency by reducing UHC emissions. Combined fuel strategies, such as E85 with biodiesel, aimed at increasing the reactivity span, have increased peak brake thermal efficiency from approximately 40% for the gasoline-diesel baseline to around 43% in a light-duty engine [4]. Hunicz et al. [10] replaced diesel HRF with highly reactive hydrotreated vegetable oil while using methane as LRF. The higher HRF reactivity halved methane emission at comparable NO_X emissions.

Despite its advantages over conventional diesel combustion, RCCI faces significant challenges related to combustion control. One of the primary concerns is control of the pressure rise rate (PRR), particularly at high loads, where excessive PRR can lead to increased combustion noise and mechanical stress. Strategies such as retarding HRF injection timing, applying EGR and increasing boost pressure have been shown to reduce PRR by increasing mixture resistance to auto-ignition and promoting charge dilution [11]. Furthermore, controlling heat release remains complex due to its strong dependence on fuel stratification and chemical kinetics [7]. Model-based control strategies have demonstrated stable operation over a wide range of engine conditions, even outside calibrated regions, provided that appropriate control variables are selected for different operating regimes [3].

However, investigations into the effects of modifications to standard diesel engine hardware are scarce. Szamrej et al. [12] concluded that RCCI combustion has been widely explored through numerical approaches, but experimental research into in-cylinder fluid motion and its influence on dual-fuel stratification, spray distribution and combustion remains limited and insufficiently validated by engine experiments.

Among engine geometry parameters, the piston bowl plays a critical role. Conventional diesel combustion with a short ignition delay (ID) benefits from strong in-cylinder mixing promoted by deep, re-entrant piston bowls. In contrast, RCCI relies on a long ID and requires stratified fuel reactivity, rather than over-mixing. In this context, Dempsey et al. [13] considered a modified diesel piston for RCCI with a shallow, wide bowl. At the same compression ratio, the modified bowl reduced the combustion chamber surface area at top dead centre (TDC) by 13%, leading to lower heat transfer losses and a more quiescent flow field, favourable for RCCI partially premixed combustion. The dedicated RCCI piston improved thermal efficiency by 2–4%, particularly at low loads, where gains in both combustion efficiency and reduced heat losses were observed. At low load, the piston modification reduced incomplete combustion losses by 3% while maintaining the same NO_X emissions. Combustion efficiency improvements diminished at higher loads, but the reduced heat transfer remained the primary driver of increased thermal efficiency.

Oh et al. [14] experimentally compared piston geometries similar to those studied by Dempsey, and additionally evaluated two injector nozzle configurations: a typical diesel nozzle and a narrow-included dual-row nozzle. The research confirmed that the shallow bowl configuration improved combustion efficiency while simultaneously reducing NO_X and smoke emissions. The effect of the nozzle modification was less pronounced, but it further reduced both emissions. Notably, the dual-row injector increased the number of fine PM.

The swirl ratio (SR) is another crucial geometry parameter in mixture formation and RCCI combustion. Investigating a high-performance conventional diesel engine, Feng et al. [15] demonstrated that while increasing SR improves combustion efficiency, indicated efficiency peaks at moderate swirl (SR = 1) due to optimal combustion phasing and duration. Heat transfer losses exhibited a non-monotonic trend, influenced by both flame penetration and near-wall flow dynamics. A moderate swirl increased in-cylinder turbulence, thereby enhancing mixture formation and improving oxygen utilisation during the mixing-controlled combustion stage. In turn, excessive swirl reduced local oxygen availability and suppressed overall heat release. Soot emissions minimised at an SR of 1. Cui et al. [16] performed an optical study of dual-fuel combustion using diesel and NG in a constant-volume chamber. Using a swirl generator, they showed that increased fluid motion improved mixing and advanced ignition. However, higher SRs led to over-homogenisation, delaying ignition.

Curran et al. [17] were the first to consider the SR effect on RCCI, using a stock swirl-control valve available on the engine. Research was conducted at a single operating point of 2,300 rpm and 0.55 MPa net IMEP. RCCI was realised with diesel as HRF and gasoline as LRF. Closing the control valve increased SR, thereby reducing the peak heat release rate (HRR); however, it had no significant effect on ID. For a blend rate of 81%, shifting SR from the lowest to the highest setpoint increased gross ITE from 41% to 43.5%. A parametric sweep of swirl valve angle for blend rates ranging from 77% to 85% revealed that improved thermal efficiency generally coincided with higher SRs, although the specific optimum varied by fuel blend rate. According to the authors, the requirement for higher SRs to reach peak efficiency and reduce emissions suggests that fuel–air premixing of gasoline, diesel, or both was initially insufficient and was improved through enhanced in-cylinder turbulence.

Kokjohn et al. [18] benchmarked diesel-gasoline RCCI realised on stock light-duty and heavy-duty compression ignition engine platforms. Both engines achieved ultra-low NO_X and soot emissions with stable combustion. However, the light-duty engine showed approximately 7% lower gross ITE than the heavy-duty platform. This difference was primarily attributed to higher heat transfer losses in the light-duty engine, driven by its higher SR (2.2 vs. 0.7) and less favourable combustion chamber geometry. Computational fluid dynamics (CFD) simulations demonstrated that reducing swirl to 0.7 and adopting a scaled heavy-duty piston bowl enabled the light-duty engine's ITE to be raised to 53%, closely matching that of the heavy-duty counterpart.

A simulation study by Yousefi et al. [19] on diesel-NG RCCI performed at low engine load and speed (brake mean effective pressure – BMEP of 0.405 MPa and 910 rpm) reported trends opposite to those observed experimentally by Curran et al. [17]. Increasing SR from 0.5 to 3.0 resulted in a monotonic decrease in fuel efficiency of approximately 10%. Heat transfer analysis confirmed that swirl enhancement intensified thermal losses, which increased by approximately 15%. The initial combustion phasing remained largely unaffected, but the peak HRR consistently declined with higher SR, and combustion became more prolonged. Late combustion termination, combined with the cooling effect of heat transfer, reduced combustion efficiency. This manifested as increased CH_4 and CO emissions, while NO_X emissions decreased, due to a more homogeneous temperature distribution. It is worth noting that for late diesel injection (which is not typical for RCCI), the effect of SR was less pronounced and non-monotonic, with a peak thermal efficiency at moderate SR. Notably, the trend was opposite at medium load (BMEP = 1.1 MPa) and medium speed (1,750 rpm).

A simulation study by Dadsetan et al. [20] investigated the effects of SR on combustion, efficiency and emissions in a heavy-duty diesel-gasoline engine. The SR was varied from 0.2 to 2.2 while maintaining a constant crank angle position at 50% fuel burnt (CA50) by adjusting the blend ratio. Gross indicated efficiency peaked around SR = 0.95, beyond which further increase in swirl elevated heat transfer, reducing efficiency. In terms of emissions, increasing SR from 0.2 to 1.2 reduced NO_X by 30%, due to lower peak temperatures resulting from improved mixture homogeneity. The trend saturated, with no noticeable improvement beyond SR of 1.2. Soot emissions were minimised at SR = 0.95, but sensitivity was barely significant. CO and UHC emissions increased steadily by approximately 500% for the case with the highest SR, attributed to flame quenching and incomplete combustion near cooler wall regions. Overall, the study identified an optimal swirl range of 0.95–1.2 to balance efficiency, combustion stability and emissions.

Another simulation study by the same group [21] examined a heavy-duty diesel-NG engine at 1,300 rpm and 0.9 MPa IMEP at the best efficiency point. The simulations explored SRs from 0.3 to 1.3, focusing on how swirl influences the in-cylinder equivalence ratio distribution. The results showed that increasing SR produced a more homogeneous in-cylinder mixture by diluting local fuel-rich regions before combustion begins. Higher SRs generally increased the ID while keeping the ignition location unchanged. Increasing the SR from 0.3 to 1.3 delayed CA50 monotonically by 18 crank angle degrees (CAD). Regarding emissions, the study found that NO_X levels decreased markedly with increasing SR, largely due to reduced high-temperature zones. However, as swirl continued to rise beyond moderate levels, incomplete combustion effects became more pronounced. Specifically, CO and UHC emissions increased due to flame quenching and local extinction, particularly in the squish regions. These effects also reduced ITE, which, however, remained above 50% for SRs between 0.7 and 0.85.

An optimisation simulation study by Yazdani et al. [22] demonstrated the combined effects of SR and start of injection (SOI) timing in split injection. The optimal SR was found to be between 0.5 and 0.6. for the investigated heavy-duty engine operating in diesel-gasoline RCCI mode at 1,300 rpm. Notably, they reported that the effect of SOI on ITE depends on the applied SR. For low SRs, an earlier SOI of the first injection resulted in higher efficiency, whereas for higher SRs, a later injection was more beneficial.

Recently, Zhou et al. [23] performed an extensive simulation study on the SR effect in diesel-ammonia RCCI. They found that, in contrast to less premixed dual-fuel combustion, the role of SR fundamentally differs under RCCI conditions. In dual-fuel mode, increasing SR from 0.5 to 3 enhanced spray breakup, shortened penetration, and reduced wall wetting, thereby improving combustion efficiency. However, the same increase in SR under RCCI conditions led to excessive mixture homogenisation. It was demonstrated that RCCI ignition was only weakly sensitive to SR during the early auto-ignition phase, whereas high SR significantly altered combustion development as the reaction propagated toward the squish region. Elevated swirl accelerated heat release but simultaneously intensified wall heat losses, resulting in lower thermal efficiency than with low-swirl conditions. The study concluded that RCCI operation requires carefully balanced swirl–tumble fluid motion control, coordinated with the injection timing strategy.

The importance of SR in conventional and RCCI combustion has been acknowledged, but a fundamental knowledge gap remains regarding the mechanisms by which SR influences combustion in RCCI engines. On one hand, swirl-driven turbulence before ignition enhances fuel–air mixing, promoting mixture homogenisation and potentially improving ignition stability. This pre-combustion effect (Phenomenon 1) is dominant when diesel injection occurs early, allowing turbulence to act on the charge before combustion initiates. On the other hand, SR also affects post-ignition combustion (Phenomenon 2) by sustaining residual turbulence, which can accelerate reaction rates and improve combustion completeness, particularly in stratified mixtures. A third mechanism involves increased convective heat transfer losses due to turbulence near cylinder walls (Phenomenon 3), which may counteract the thermal efficiency benefits gained from faster combustion. These are recognised effects, but their relative importance and interactions, particularly with respect to injection timing, remain insufficiently understood under realistic engine conditions. Consequently, the present study addresses the following research gaps:

(i) lack of experimentally validated understanding of the coupled effects of SR and injection strategies in RCCI operation,
(ii) limited insight into the distinct roles of swirl- and tumble-induced flow structures in governing ignition and combustion development,
(iii) insufficient linkage between in-cylinder flow phenomena and emission formation mechanisms under dual-fuel conditions.

This study's central hypothesis is that there is a local optimum in SR, defined by the trade-off between improved reactivity stratification and the onset of over-homogenisation or increased wall cooling. This optimum is highly dependent on the timing of diesel injection and the combustion chamber design. Specifically, early injection allows SR to affect stratification significantly, whereas its influence should diminish at later injections. The study investigates this coupling between SR and SOI using a systematic experimental matrix in a diesel-natural gas RCCI engine. By controlling SR and SOI independently, the CFD-supported engine experiments provide new insight into the timing-sensitive role of in-cylinder turbulence in shaping combustion phasing, heat release and emissions. The work offers critical guidance for RCCI engine calibration and design optimisation.

2. Experimental and numerical methods

This section outlines the study's experimental and numerical methodology. It includes the research engine and fuel specifications, measurement systems and operating conditions, followed by the procedures used for data processing and analysis. It concludes with a discussion of the CFD approach used to simulate in-cylinder flow and support the interpretation of experimental results.

2.1. Research engine

A state-of-the-art single-cylinder research engine (AVL 5402) served as the experimental platform for investigating the combined effects of SR and SOI of HRF. Table 1 lists the key engine specifications. A schematic diagram of the engine test stand is provided in [10].

The combustion system featured a four-valve cylinder head and a toroidal combustion chamber integrated into the piston. A Bosch CP 4.1 high-pressure pump delivered HRF through an eight-hole solenoid injector with a spray cone angle of 151°. Fuel pressure and injection timing were managed using ETAS INCA software in conjunction with an open Bosch control unit.

Table 1
Research engine data.

Type	AVL 5402
Configuration	four-stroke, single-cylinder
Bore	85 mm
Stroke	90 mm
Connecting rod length	138 mm
Displacement	510.5 cm^3
Compression ratio	17:1
No. of valves	four
Swirl ratio	variable with intake port configurations – see Fig. 1 and Table 2
Diesel injection system	direct, common rail, Bosch CP4.1
Fuel injector	electromagnetic, eight-hole x 0.12 mm, 151° incl. angle
Max. fuel injection pressure	180 MPa
NG fuelling system	mass flow controller, M + W Instruments D-6300
Boost system	electrically driven Eaton M45 compressor
Engine management	AVL-RPEMS, ETK7-Bosch
Intake valve opening	712 CAD
Intake valve closing	226 CAD
Exhaust valve opening	488 CAD
Exhaust valve closing	18 CAD
Max. engine IMEP	2.4 MPa

Gaseous LRF was introduced at a steady rate via a calibrated mass-stream D-6300 flow controller (M + W Instruments). The gas was premixed with intake air in a plenum chamber to ensure uniform distribution before entering the cylinder. Intake air was pressurised using an Eaton M45 Roots-type supercharger driven by an electric motor. Downstream air temperature was stabilised through a heat exchanger system and a mixing valve. A backpressure valve installed in the exhaust line mimicked turbocharger operation, additionally preventing gaseous fuel scavenging during valve overlap.

SR control was a central focus of this study. To this end, the cylinder head featured AVL's proprietary split intake port design, incorporating tangential, helical and neutral ports to enable variable swirl generation. Fig. 1 illustrates how SR was modulated by selectively blocking intake ports using blanking plates. Table 2 summarises the intake port configurations and corresponding SRs. It is worth noting that SR is defined as the ratio of in-cylinder fluid rotational speed to engine rotational speed. The SR data for cases B-D were provided by the engine manufacturer, while for all the cases, the SR, along with other in-cylinder flow parameters, was redundantly determined via CFD flow simulations. Table 2 shows the applied port configurations and the manufacturer-referenced (measured) SR values.

It should be noted that different port configurations affect not only SR but also other in-cylinder fluid motion parameters, e.g., tumble intensity and the distribution of turbulent kinetic energy (TKE) within the cylinder. However, SR is used consistently throughout the paper as a parameter to distinguish between different port configurations, as the variable intake system was primarily designed to control SR.

2.2. Measurement instrumentation and procedures

Cylinder pressure was measured using an AVL GU22C piezoelectric pressure sensor, connected to a dedicated charge amplifier and triggered by an optical encoder. Data acquisition was performed with a crank angle resolution of 0.1 CAD to capture detailed combustion dynamics.

Exhaust gas analysis was conducted using an AVL Fourier transform infrared (FTIR) analyser, capable of simultaneously quantifying 20 regulated and unregulated gaseous species. Particle number (PN) and size distribution were measured with a TSI EEPS 3090 spectrometer. This system provided size-resolved particle data across 32 channels, ranging from 5.6 to 560 nm. Table 3 outlines the key specifications of the instrumentation used.

Process variables, such as air and fuel mass flow rates, temperatures, excess air ratio (λ) and average intake and exhaust pressures, were recorded using an in-house data acquisition system. The diesel mass flow rate was measured using an AVL 733S fuel consumption meter, while the natural gas LRF consumption was monitored directly through the mass flow controller.

In-cylinder pressure was recorded for 100 cycles at each steady-state

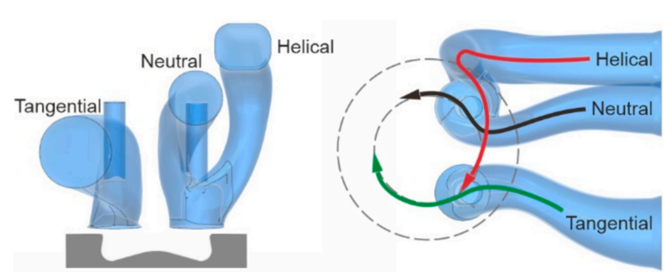

Fig. 1. The side view (left) and top view (right) of intake channels showing the swirl control concept.

Table 2
Port configurations for swirl control.

Case	Tangential	Neutral	Helical	SR meas.
A	Closed	Open	Closed	ND
B	Open	Open	Open	1.7
C	Open	Closed	Open	2.9
D	Closed	Closed	Open	4.5

Table 3
Measurement equipment and accuracy.

Quantity	**Transducer**	**Meas. range**	**Accuracy**
In-cylinder pressure	AVL GU22C	0–25 MPa	0.25–1.0%[a]
IMEP stability		N/A	3%
Liquid fuel consumption	AVL Fuel Mass Flow Meter 733S	0–125 kg/h	0.12%
Gaseous fuel consumption	M + W Instruments D-6300	0–120 Nl/min	2%
Excess air ratio (λ)	Bosch LSU 4.2 / ETAS LA4	0.7–2.8	1.5%
Air mass flow rate	E + E Elektronik EE741	2.6–1000 kg/h	3%
Intake/exhaust press.	WIKA A-10	0–4 bar	0.5%
Temperatures(ambient, intake air, cooling, oil, fuel)	Pt100 Czaki TP-361	−40–400 °C	0.2%
Exhaust temperature	Thermocouple K Czaki TP-204	0–1200 °C	0.8%
Exhaust composition (gaseous compounds)	AVL Sesam FTIR CO: HC: NO_X:	1–10000 ppm 1–1000 ppm[b] 1-4000 ppm	0.36% 0.1–0.49%[c] 0.31%
PM/PN	TSI EEPS 3090	5.6–560 nm[d]	N/A

[a] Depending on temperature.
[b] Given measurement span relates to the concentration of a single identified hydrocarbon
[c] Depending on the type of hydrocarbon species.
[d] Particle size range.

engine operating point. All slow-changing parameters, including exhaust composition, were recorded synchronously with pressure acquisition for 30 s and automatically averaged.

2.3. Fuels

The HRF used was a commercially available European pump-grade diesel conforming to EN 590 standard, produced by the Polish oil company Orlen. It contained 6.3% fatty acid methyl esters, had a lower heating value (LHV) of 43.6 MJ/kg, and a derived cetane number of 50. The LRF was technical grade methane 2.5, supplied by Linde, with a CH_4 concentration of at least 99.5%. Given its high purity, the methane's physical and chemical properties were not individually analysed. Methane LHV of 50 MJ/kg was assumed for thermal efficiency analyses. The gaseous fuel is referred to as NG throughout this study.

2.4. Experimental conditions

Testing was conducted at a single engine speed and load setpoint of 1,500 rpm and approximately 0.8 MPa IMEP, subject to changes in thermal efficiency (constant fuel value across all sweeps). The total energy introduced to the cylinder was 948.5 ± 6.6 J with an NG energy fraction of 80% ± 0.58%. Diesel fuel injection pressure was set at 100 MPa. The SR and the diesel SOI (single injection) were the sole parameters regulated during the experiments. As shown in Table 2, SR was controlled by opening or closing intake ports using dedicated blanking plates. Boost pressure was set to 141 ± 0.5 kPa with all intake ports open, but was slightly elevated to compensate for the pressure drop when selected ports were closed, to achieve the same mass of aspirated air (731 ± 16 mg). This yielded a constant λ of 2.25. Note that the precisions provided here are double standard deviation values from multiple measurements at the parameter sweeps.

All experiments were performed at stable engine coolant and oil temperatures, both set to 85 ± 0.5 °C, while intake air temperature was set to 26 ± 1 °C.

2.5. Experimental data processing methods

The raw in-cylinder pressure signal was pegged using the exhaust pressure as a reference, ensuring accurate estimation of combustion parameters. Combustion analysis was performed cycle by cycle over 100 individual cycles, after which key parameters were averaged and statistically evaluated.

Gross IMEP, defined over a single crankshaft revolution between consecutive bottom dead centres (BDCs), was used to calculate ITE, based on LHV-weighted fuel consumption of both fuels. In single-cylinder laboratory engines, indicated-specific-based metrics are considered more reliable than brake-specific ones typically used in multi-cylinder setups. Accordingly, all power-based values in this study are reported as gross indicated-specific.

The uncertainty in ITE was evaluated using total differentiation, incorporating measurement errors in fuel flow rates (for both diesel and NG) based on the standard deviation across repeated measurements. The dominant source of error was the uncertainty in IMEP, as specified by the pressure sensor manufacturer (see Table 3). The maximum total ITE uncertainty across all cases was estimated at 3.3%.

Crank-angle-resolved HRR (ΔQ/Δα) was calculated using a first-law thermodynamic analysis:

$$\frac{\Delta Q}{\Delta \alpha} = \frac{\gamma}{\gamma - 1} p \frac{\Delta V}{\Delta \alpha} + \frac{1}{\gamma - 1} V \frac{\Delta p}{\Delta \alpha} \tag{1}$$

where p and V are in-cylinder pressure and volume, respectively. The instantaneous specific heat ratio (γ) was determined as a function of gas temperature and composition. The in-cylinder gas temperature was derived from the measured pressure using the ideal gas law, with the evolving HRR used to dynamically update the mixture composition. The HRR values presented are net, incorporating heat loss to the cylinder walls, estimated via the Hohenberg correlation [24]. Notably, heat transfer coefficients were not adjusted for swirl-induced effects. Cumulative net heat release was used to determine key combustion phasing indicators, specifically the crank angles at which 5% and 50% of the fuel mass was burned (CA05 and CA50, respectively).

Exhaust species concentrations were converted to gross indicated-specific emissions based on atomic fuel composition, λ, and specific fuel consumption. PM and PN emissions were calculated from measured size distributions, assuming a particle density of 1 g/cm^3. The directly measured volumetric concentrations were subsequently converted into gross indicated-specific values.

An overlimit function (f) in Eq. (2) was developed to analyse the overall effect of SR and SOI on RCCI performance:

$$\begin{aligned} f = \sum \max\left(0, \frac{E_i}{E_{\text{norm}}} - 1\right) W + \max\left(0, \frac{50\%}{\text{ITE}}\right) \times 100 \\ + \max\left(0, \frac{\text{CoV(IMEP)}}{5\%} - 1\right) \times 10 \end{aligned} \tag{2}$$

In this formulation, E_i represents the emissions of a specific exhaust component i, normalised by its corresponding regulatory limit E_{norm} in accordance with EU Stage V standards for stationary engines with a power rating ≥ 130 kW. For CH_4 emissions, limits applicable to gas engines were adopted. The emission weighting factors W were selected arbitrarily.

The weighting factor for CH_4 was set to 2, based on the premise that NO_X, CO, and non-methane hydrocarbons (NMHC), each assigned a unity weighting, can be relatively readily reduced or oxidised using available aftertreatment technologies [25]. In contrast, robust methane-oxidation catalyst technologies are not yet well established [26], particularly for low-temperature dual-fuel combustion. In such conditions, performance is hindered by high light-off temperatures [9], and even small amounts of sulphur can effectively deactivate the catalyst, with regeneration remaining challenging [27].

The reference values for ITE and for coefficient of variation (CoV) in IMEP were set to 50% and 5%, respectively. The latter value forms an acceptable limit for stable engine operation. It should be noted that ITE in Eq. (2) was corrected to 100% combustion efficiency, to avoid consideration of hydrocarbons and CO emissions twice in the over-limit function.

2.6. Simulation of in-cylinder fluid motion

The 3D CFD simulations of in-cylinder flow were performed to provide background for the discussion of the experimental results. Intake and exhaust pressures and temperatures were held constant during the simulations, matching the experimentally measured values. The temperatures of the cylinder head, liner and piston were maintained at 420, 450 and 500 K, respectively. Large eddy simulation was adopted to resolve the turbulent flow field. Dynamic mesh refinement was employed, with grid adjustment according to the local gas velocity in each cell. For example, in case D, the total cell number varied from 615,414 at 230 CAD before top dead centre (bTDC) to 136,369 at 40 CAD bTDC.

SR was determined from CFD results based on angular momentum and moment of inertia, integrating contributions from all fluid cells within the cylinder to quantify the airflow's overall rotational motion [28]. The tumble ratio was calculated in this study using a three-dimensional approach based on angular momentum, in which rotation is evaluated about the system's centre of mass using rigid-body dynamics. TKE of the computational cell were defined as the mean kinetic energy per unit mass associated with turbulent velocity fluctuations. TKEs for specific regions (bowl or squish) were calculated as volume-weighted averages.

The detailed description of governing equations used for in-cylinder flow parameters calculations, under the above assumptions is provided in Appendix A.

3. Results

This section presents the results, combining numerical and experimental analyses to evaluate the effects of intake port configuration and injection timing. It begins with a characterisation of in-cylinder flow and spray interaction, followed by an assessment of ignition behaviour and heat release. The influence of swirl on fuel stratification, combustion progress, efficiency and cyclic variability is then examined. Finally, the impact on exhaust emissions is analysed, and the overall performance is evaluated using an overlimit function.

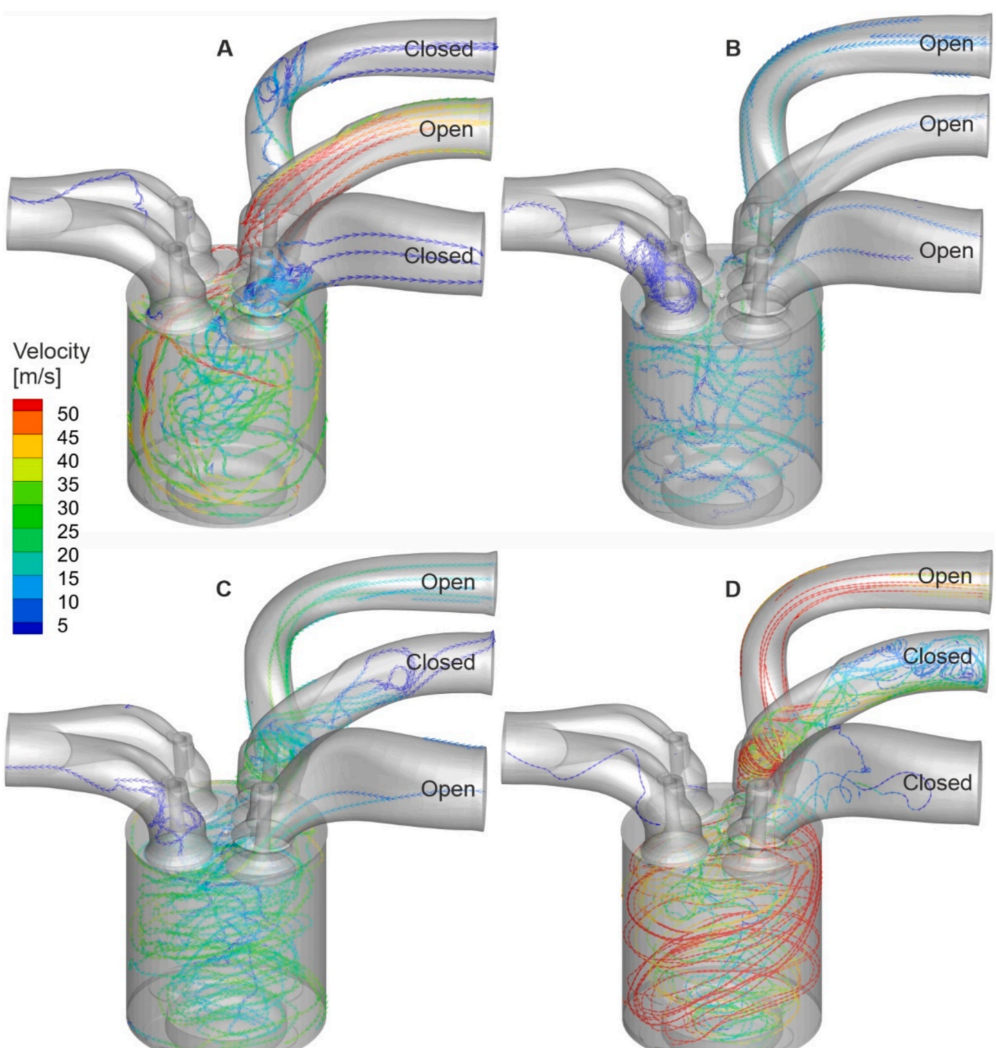

Fig. 2. Visualisation of intake flow for all investigated intake port configurations.

3.1. In-cylinder gas motion simulations and injection patterns

The experimental findings were complemented by CFD simulations, which provided additional insight into in-cylinder fluid motion and supported the interpretation of the measured data. Fig. 2 illustrates the flow rates through the intake ports and inside the cylinder at BDC between the intake and compression strokes. Fig. 3 presents fluid velocity maps at 42 CAD bTDC, which corresponds to a timing close to the HRF injection event. Consistent with the design configurations shown in Fig. 1, case A is generated with only the neutral intake port open, and results in an anticlockwise swirl motion. Conversely, the tangential and helical intake ports are associated with clockwise swirl motion, with flow velocities corresponding to the predetermined SR values (SR = 2.9 and SR = 4.7, respectively). The cumulative swirl effect from all ports open (case B) outweighs the anticlockwise flow from the neutral valve, resulting in SR = 1.7. Importantly, regardless of the swirl or tumble motion, the vortex centres are in the piston bowl, while higher-velocity airflow is distributed in the squish region. Compared to other configurations, the velocity field in the quiescent condition is more uniformly distributed before diesel injection, with only a small low-velocity zone forming near the centre of the cylinder. In the other SR control schemes, as the SR increases from 1.7 to 4.5, the swirl velocity in the squish region gradually rises from generally below 15 m/s to over 25 m/s. However, a large low-velocity zone persists in the cylinder's central region.

Table 4 quantifies flow parameters defined in Subsection 2.6 at two characteristic crank positions: at intake valve closing effect (IVC) and at SOI = 42 CAD bTDC. Comparing the SR values at IVC with the engine manufacturer's data shows that simulation results are 0.5 to 0.7 lower than the measured reference. It should be noted that SR is not rigorously defined, and its value is method-dependent. However, the manufacturer's and CFD-derived values show good correlation, with an approximately constant offset. However, both manufacturer-provided and CFD-derived values correlate well, with nearly constant offset.

According to Table 4, SR is only weakly attenuated during the compression stroke, exhibiting minimal decay. The tumble ratio evolves nonlinearly as the centre of rotation shifts and is further influenced by the squish phenomenon. In contrast, TKE is strongly dependent on intake air velocity. Consequently, higher TKE values are observed in cases A and D, where only one intake port is open, compared to cases B and C, where both intake ports are open.

Fig. 4 shows the interactions between the developing spray and the combustion chamber at characteristic crank angles. The crank angles of 25 CAD bTDC and 19 CAD bTDC correspond to piston positions shortly before the onset of low-temperature reactions for the HRRs presented in Fig. 5. The high-pressure injection duration is short (approximately 3 CAD) due to the relatively small quantity of liquid fuel in RCCI operation, and the spray fully evaporates before reaching the liner.

Table 4
Indicators of in-cylinder flow characteristics.

Indicators	Timing	Case A	Case B	Case C	Case D
Swirl ratio (SR)	IVC	1.85	1.01	2.15	4.03
	SOI	1.78	1.00	2.08	3.72
X-axis tumble ratio	IVC	0.05	0.31	0.06	0.21
	SOI	0.23	0.10	0.23	0.09
Y-axis tumble ratio	IVC	0.57	0.31	0.29	0.10
	SOI	0.16	0.22	0.03	0.11
TKE in bowl (m^2/s^2)	IVC	18.96	8.20	7.04	14.90
	SOI	7.94	5.37	4.44	5.40
TKE in squish (m^2/s^2)	IVC	11.1	5.21	4.17	6.91
	SOI	3.84	3.01	2.40	2.28

Fig. 4 also shows that at an SOI of 40 CAD bTDC, the fuel spray is primarily distributed in the squish region, with limited penetration into the piston bowl. Mixture homogenisation appears more effective in cases A and D than in the other configurations. Notably, these two cases operate with only a single intake port open, which enhances TKE in both the bowl and squish zones. It should be noted that after injection, tumble flow intensifies as the piston moves upwards due to the squish effect. At the same time, the swirl component, introduced by the intake valve geometry, dissipates. Under nominal conditions, this dynamic promotes redistribution of the high-reactivity fuel toward the cylinder centreline.

Figs. 3 and 4 provide context for interpreting Phenomenon 1 – the effect of swirl-enhanced mixing before ignition – and form the basis for a critical assessment of ignition behaviour and combustion development in the following sections. The key takeaway is that modifying the intake port structure influences not only the in-cylinder flow field but also the evolution of the in-cylinder reactivity field.

3.2. Qualification of swirl-induced phenomena based on experimental heat release rates

Fig. 5 presents the experimental HRR profiles (calculated according to Eq. (1) as a function of crank angle for four different swirl regimes. The curves reveal distinctive differences in the temporal evolution and intensity of combustion.

In cases B-D, where the in-cylinder flow motion is clockwise, one can note that, for the given SOI, the highest SR supports optimal reactivity stratification while avoiding over-homogenisation of the mixture near the cylinder walls. Lower SRs result in significantly increased combustion delay (over 5 CAD – refer to Fig. 6). Interestingly, the combustion progress for cases B and C, with SR 1.7 and 2.9, is statistically identical.

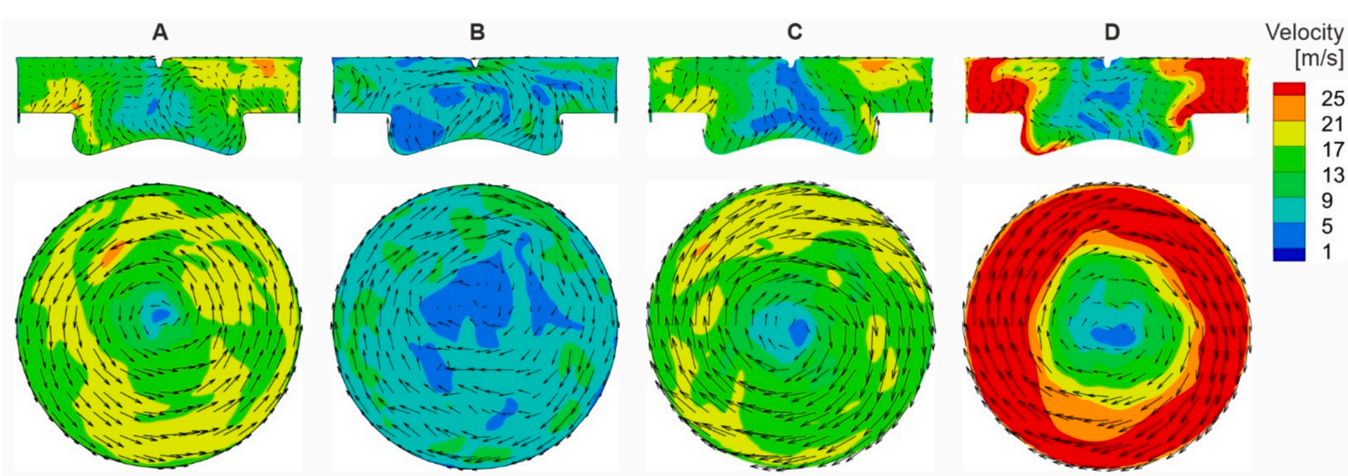

Fig. 3. In-cylinder fluid motion velocity at 42 CAD bTDC: the SR values correspond to different intake valve opening strategies, as listed in Table 2 and shown in Fig. 2.

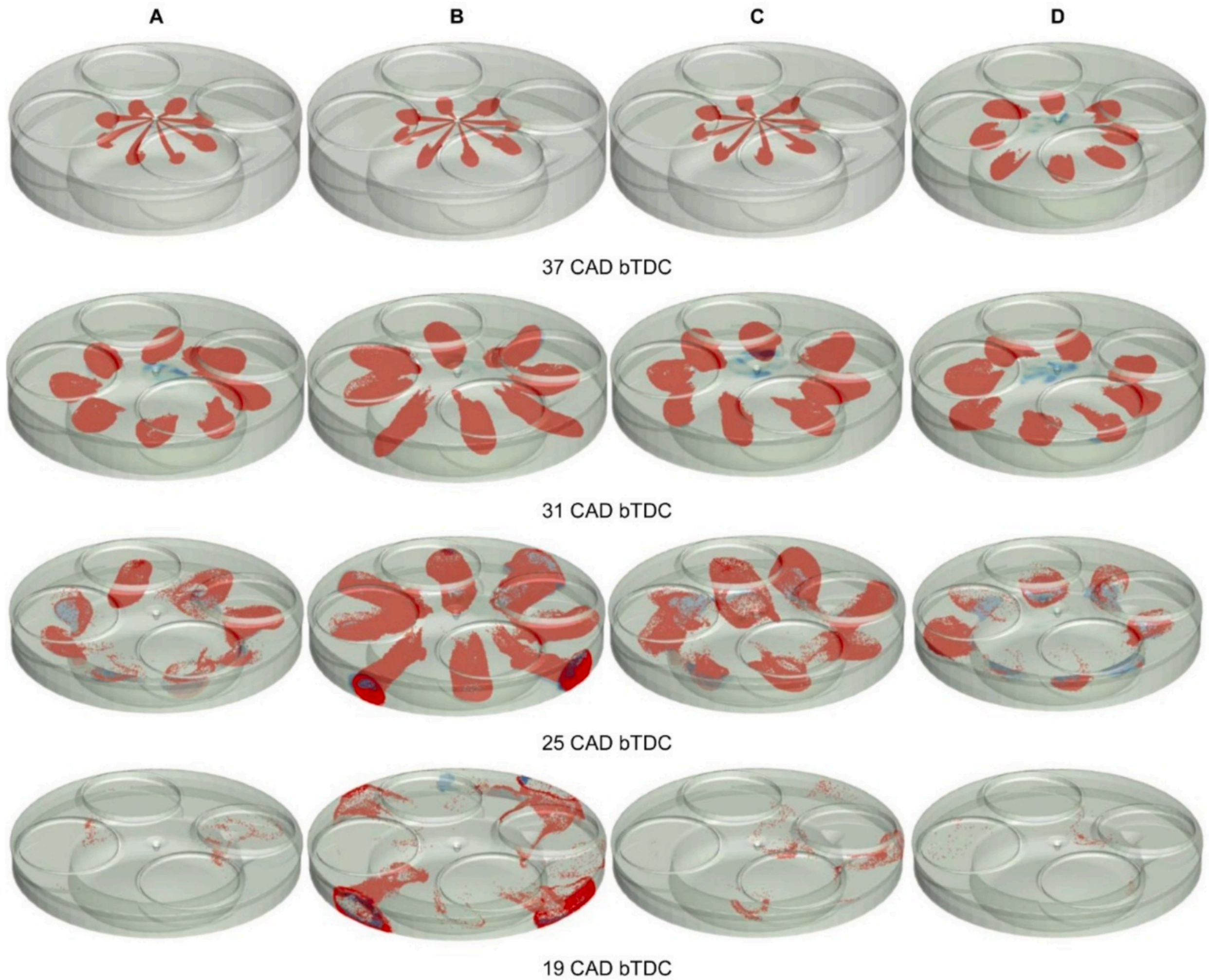

Fig. 4. Spray-combustion chamber interactions at the characteristic crank angle positions for SOI = 40 CAD bTDC.

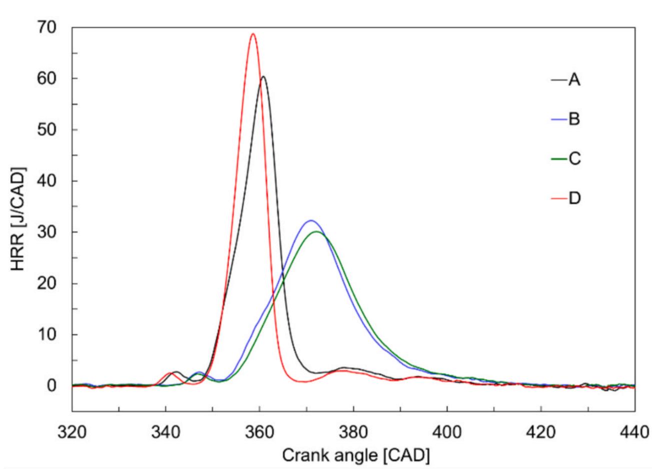

Fig. 5. HRR for SOI = 40 CAD bTDC and variable SR.

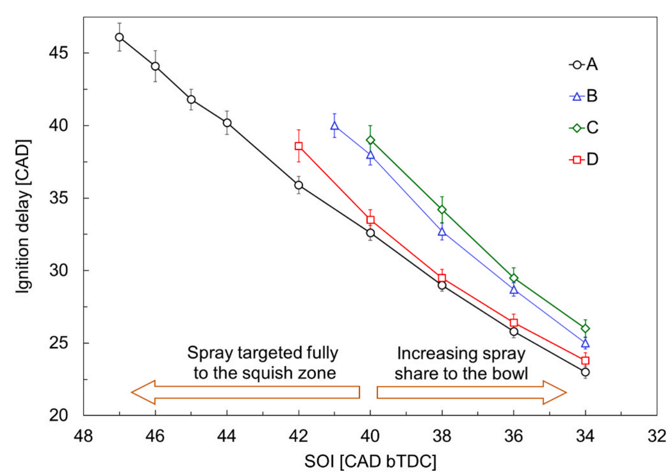

Fig. 6. Ignition delay (the angular distance between SOI and CA05) versus SOI: error bars show standard deviations of CA05 calculated for 100 consecutive cycles.

This implies that port-induced swirl largely quenches near TDC. In other words, as soon as the combustion is phased after TDC, the influence of SR on post-ignition processes (Phenomenon 2) remains negligible. Consequently, for case D with SR = 4.5, the significantly faster heat release likely results from the superposition of two mechanisms: increasing temperature and pressure during compression, which enhance chemical kinetics; and swirl-induced fluid motion sustained by the squish-driven flow field, which accelerates reactant entrainment.

Case A reveals a noteworthy non-monotonicity. Although the flow velocities are similar to case C, but in the opposite direction, it exhibits equally short ID as case D (SR = 4.5), which deviates from the expected progression. This may point to additional flow phenomena not captured by SR alone. One possible explanation is the effect of tumble flow components, especially within the bowl geometry, which enhances early local mixing or turbulence near ignition zones. Alternatively, localised flow structures, manifested by increased TKE within the bowl (see Table 4), may accelerate ignition through intensified mixing in isolated diesel-jet regions. The last hypothesis is consistent with results from the constant-volume chamber experiments by Cui et al. [16]. The relative contribution of these effects cannot be conclusively determined at this stage, but further analysis in the following sections will aim to quantify their respective influence.

3.3. Quantifying the effect of swirl on fuel stratification and ignition

The effects of different flow patterns are further quantified in Fig. 6, which plots ID as a function of diesel SOI across the tested swirl configurations. As expected for the RCCI regime, ID decreases monotonically with retarded injection timing, driven by increased reactivity stratification. More explicitly, with later injection, highly reactive diesel fuel has less time to premix, resulting in locally richer regions which are more prone to auto-ignite.

The range of each SOI sweep in Fig. 6 is bounded by misfire limits. The right-hand cut-off is attributed to insufficient premixing at late SOIs, where HRF directed to the squish zone (Fig. 4) fails to penetrate the combustion bowl, leading to incomplete ignition in the central regions. The fact that the cut-off is sharp at the same SOI of 34 CAD bTDC, independently of the flow configuration, supports the hypothesis that the influence of port-induced motion on fuel mixing diminishes after the reference point (SOI = 40) visualised in Fig. 4. This is further evidenced by ID's convergence for all SR configurations towards the late injections.

The picture is different on the left-hand side of Fig. 6. The neutral port configuration (case A) evidently extends the range of stable RCCI operation towards early injections. The cases with clockwise swirl enter misfire consistently at SOIs between 42 and 40 CAD bTDC. This is caused either by overleaning the reactive fuel, which is subjected to intensive mixing, or by the reactive spray failing to propagate towards the bowl and remaining trapped near the cold cylinder liner due to the centrifugal force of the swirl-induced flow. The fact that case A exhibits this limit for SOIs more than 5 CAD earlier, despite larger reference swirl flow velocities compared to case B (SR = 1.7), substantiates the hypothesis that extended tumble motion and TKE (refer back to Table 4) play an essential role in achieving a proper, more monotonic, fuel stratification towards the cylinder centreline, particularly for cases with very early injection.

Within the stable combustion envelope, the effect of SR on ID remains consistent across the SOI sweep, with a nearly uniform offset of approximately 5 CAD observed between case D (SR = 4.5) and the lower-swirl cases. However, Fig. 6 shows that the difference between case D and case A configurations is not statistically significant. Notably, both configurations with the earliest ignition (cases A and D) utilise only one open intake channel. This suggests that flow motion beyond swirl, such as local turbulent structures or directed jet flows, exerts a more direct influence on RCCI ignition.

The key takeaway from this section is that, under the current setup, the direct influence of swirl motion on RCCI auto-ignition appears secondary. This is due to the majority of HRF being injected into the squish region, where swirl mainly governs jet-to-jet interactions. Given sufficient premixing time, all swirl configurations effectively distribute fuel radially within the squish zone. As a result, it is the interaction between swirl and other flow structures, particularly turbulence, which plays a more decisive role by facilitating the transport of reactive fuel toward the hotter cylinder centreline, thereby exerting the greatest influence on ignition timing.

3.4. The impact of swirl ratio on combustion progress

While ID shows only a limited direct correlation with SR, the heat release profiles discussed in Subsection 3.2 suggest that combustion progression may still be affected by SR through mechanisms beyond ID. In particular, the slow combustion observed for cases B and C (SR = 1.7 and SR = 2.9) in Fig. 5 is largely attributed to their late ignition phasing, which shifts the reaction into the expansion stroke, where lower in-cylinder temperatures suppress reaction rates. Fig. 7 plots CA50 (combustion onset) as a function of CA05 (ignition onset), rather than SOI, thus isolating the effect of swirl-driven mixing on combustion progress from the confounding influence of in-cylinder thermodynamic conditions.

The error bars in Fig. 7 represent the standard deviation of CA05 and CA50, based on 100 cycles. The start of combustion and its phasing in RCCI are highly sensitive to boundary conditions; even small variations in boundary conditions, such as those allowable by the testbed control system (order of ± 1 °C in air, coolant, lube, or fuel temperatures), can lead to notable shifts in ignition timing [29]. These stochastic fluctuations have a greater impact than cumulative errors from the pressure transducer and crankshaft encoder (discretisation error), which contribute to the CA05 and CA50 calculations.

A clear correlation between SR and combustion progress can be observed in Fig. 7, particularly for cases where the combustion duration (CA50 – CA05) remains below 12 CAD. Within this range, a statistically significant trend emerges: the fastest combustion occurs at the highest SR (case D), followed by case C, and the slowest at case B. Notably, case A follows this trend, despite featuring a reversed flow direction. When considering only the magnitude of radial flow velocities (refer to Fig. 3), case A lies between cases B and C (SR = 1.7 and SR = 2.9, respectively), which aligns with its intermediate combustion duration in Fig. 7.

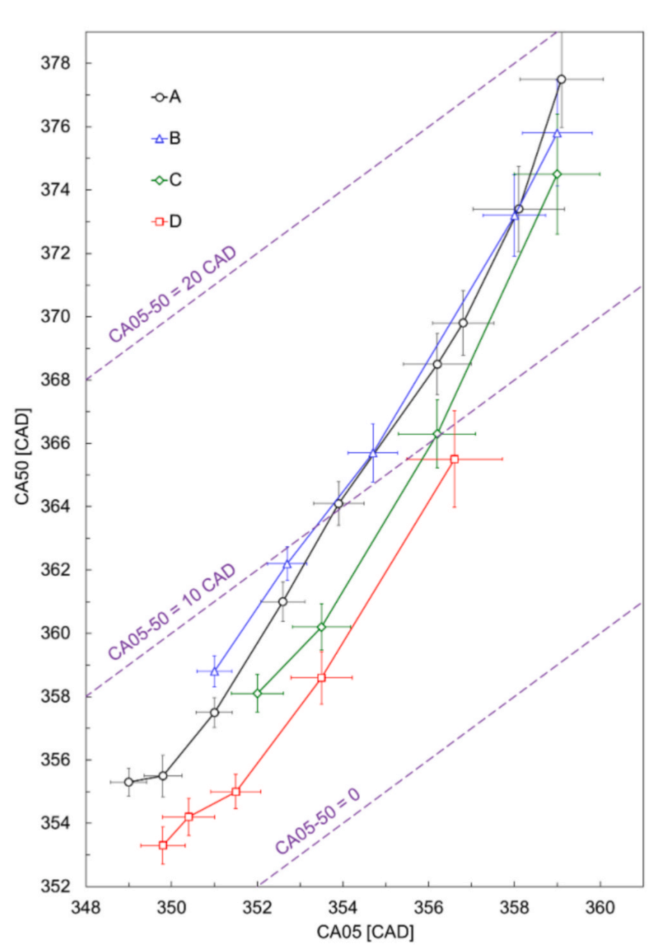

Fig. 7. CA50 versus CA05: error bars show standard deviations calculated for 100 consecutive combustion cycles.

Beyond the 10–12 CAD combustion duration threshold, the curves converge across swirl configurations. For example, at CA05 values of 358 CAD and later, differences in both CA05 and CA50 among the swirl cases become statistically insignificant. This convergence corresponds to late injection timings, where the fuel spray is increasingly directed into the piston bowl, thereby reducing the influence of swirl on mixture formation. Simultaneously, the diminishing intensity of intake-generated flow structures during the expansion phase (when CA50 exceeds ~ 365 CAD) further reduces the effect of swirl on heat release.

The above statement finds confirmation in Fig. 8. For CA50 values beyond TDC, the HRR data points across all SRs converge within overlapping uncertainty bounds. This proves that, during the expansion stroke, the lower in-cylinder temperature becomes the dominant factor controlling reaction rates, rendering the initial swirl-induced mixing effects irrelevant.

For CA50 values earlier than 365 CAD, the peak HRRs of case A diverge from the otherwise consistent trend observed across the swirl configurations. Cases D, C and B (SR = 4.5, 2.9, and 1.7, respectively) follow a clear swirl-intensity correlation, with stronger swirl yielding higher peak HRR, but case A does not fit this pattern. In this region, case A peak HRRs are higher than expected based on its lower radial flow velocity (as shown in Fig. 3). Notably, at the investigated engine load, the pressure rise rate did not exceed 0.57 MPa/CAD.

This deviation can be understood by considering the combustion phenomenology and case A's distinct flow topology. Unlike swirl-dominated flows that concentrate momentum tangentially and radially, the neutral-port-only configuration generates a more persistent local turbulences, as previously identified in Table 4. This turbulent motion enhances vertical entrainment and jet penetration toward the cylinder centreline, promoting more favourable reactivity stratification in the early combustion phase. Consequently, while swirl-dominated configurations rely on azimuthal transport and jet-to-jet interactions within the squish region, case A achieves effective fuel–air mixing through a more direct axial redistribution of reactive zones.

Variation in peak HRR and its location, shown in Fig. 8, directly translates into CoV in IMEP, shown in Fig. 9. However, comparing the two graphs reveals that the major factor determining cyclic variability is combustion timing. Fig. 9 shows that, although SR determines combustion timing, it does not significantly affect CoV in IMEP. CA50 appears to be the sole factor affecting variability. Independent of SR configuration, for CA50 < 373 CAD, CoV in IMEP is within the 5% stability limit.

Fig. 10 provides further insight into the interactions among combustion phasing, flow structure, and energy conversion. At early CA50 (< 365 CAD), case A consistently achieves the highest combustion

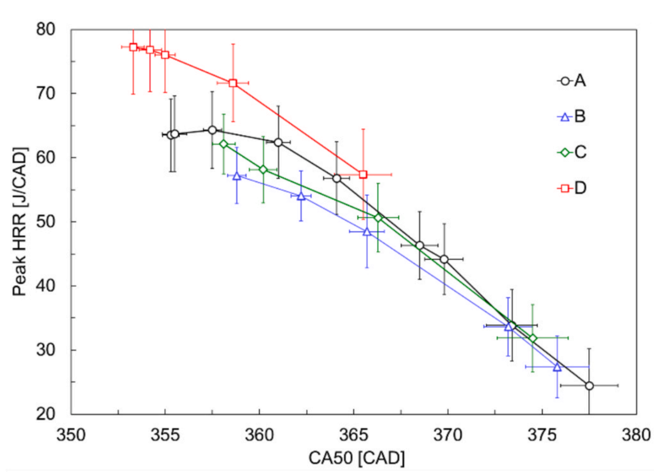

Fig. 8. Peak HRR versus CA50: error bars show standard deviations calculated for 100 consecutive combustion cycles.

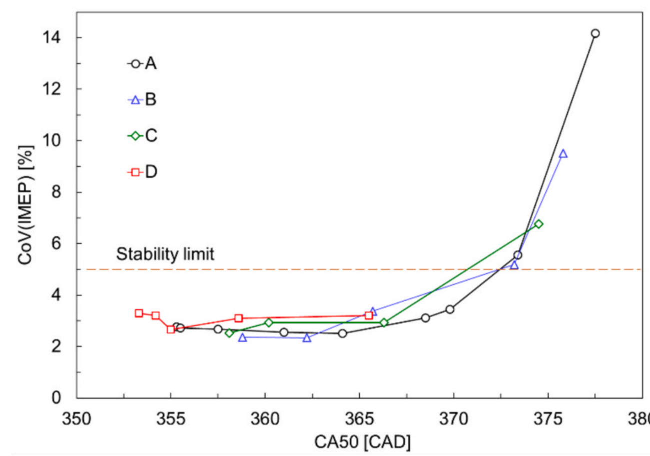

Fig. 9. CoV in IMEP versus CA50.

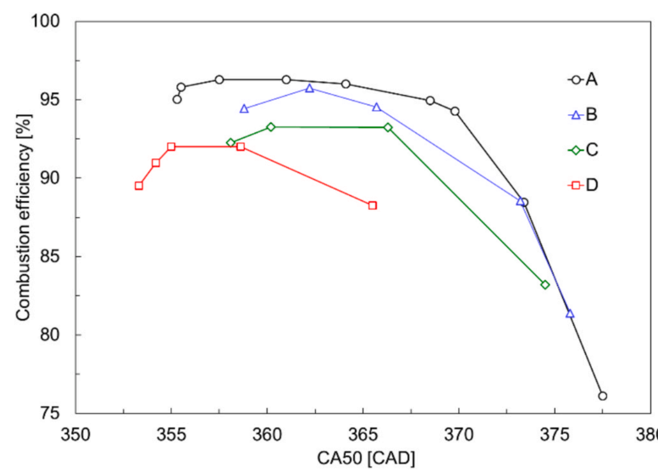

Fig. 10. Combustion efficiency versus CA50.

efficiency, despite lacking a strong swirl. This is consistent with earlier observations (Figs. 7, 8) showing that case A benefits from effective turbulence-enhanced reactivity redistribution and high peak HRR, both of which support complete and centralised combustion when timed early in the cycle.

In contrast, the high-swirl case D (SR = 4.5) shows the lowest efficiency in this regime, despite its fast combustion and high peak HRR. This suggests that overly intense radial mixing may lead to excessive heat transfer to colder boundary layers or poor fuel–wall targeting, as previously hypothesised. This supports the notion that while swirl accelerates combustion, it may also induce over-homogenisation or cause incomplete utilisation of reactive zones, especially when injection is already optimised for stratified operation.

As combustion phasing moves later (CA50 > 370 CAD), efficiencies drop sharply across all configurations, confirming that thermal conditions become dominant and that neither swirl nor tumble can compensate for reduced in-cylinder temperatures. Case A's steep decline at late CA50 mirrors the HRR and CA50 trends, further validating that flow-structure effects are effective only when combustion is initiated early and decay rapidly as the thermodynamic environment degrades.

It is also worth noting that in none of the tested cases did the combustion efficiency exceed 97%. This is typical of RCCI combustion, where a small fraction of unburned fuel remains due to charge trapped in cold crevices or escaping during the valve overlap period. These losses are largely unaffected by in-cylinder flow structures and represent an inherent limitation of RCCI rather than a mixing deficiency.

Combustion efficiency contributes significantly to overall ITE. This is shown in Fig. 11 to complement the previous discussion on the effect of flow patterns on RCCI combustion.

As expected, ITE peaks when CA50 occurs slightly after TDC, aligning with the optimal thermodynamic conditions for converting heat release into useful work [30]. However, beyond phasing, ITE does not always correlate directly with combustion efficiency or combustion duration. For instance, case B (SR = 1.7) achieves the highest ITE despite slower combustion than case A, which has a combustion efficiency comparable to that near the CA50 optimum. Conversely, case D (SR = 4.5), despite resulting in the fastest combustion and the highest peak HRR near optimal phasing, fails to recover efficiency due to lower combustion completeness. This suggests that strong swirl induces additional thermal losses, likely via enhanced convective heat transfer to cylinder walls – a well-documented second-order effect of elevated in-cylinder flow. This loss mechanism adds to the trade-off already discussed between mixing quality and combustion completeness.

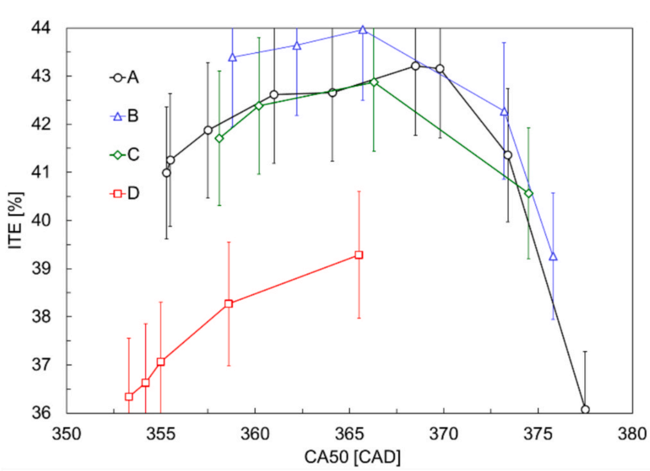

Fig. 11. Gross indicated thermal efficiency versus CA50: error bars show maximum absolute uncertainty.

3.5. Cross-validating the SR effects with emission analysis

CH_4 emissions are the main source of combustion losses in diesel-NG RCCI. Fig. 12 shows a direct correlation of CH_4 emissions with SR: the higher the SR, the higher the unburned methane. This correlates with the combustion efficiency results in Fig. 10, discussed comprehensively in the preceding section, so no further phenomenological discussion is needed. When considering the absolute emission levels, case A's RCCI can meet the stringent EU Stage V HC emission limits for gas engines. This is usually very difficult on an engine-out basis. In this context, note from Fig. 13 that the contribution of NMHC to the EU Stage V limit is of an order of magnitude lower than that of CH_4, but still statistically significant.

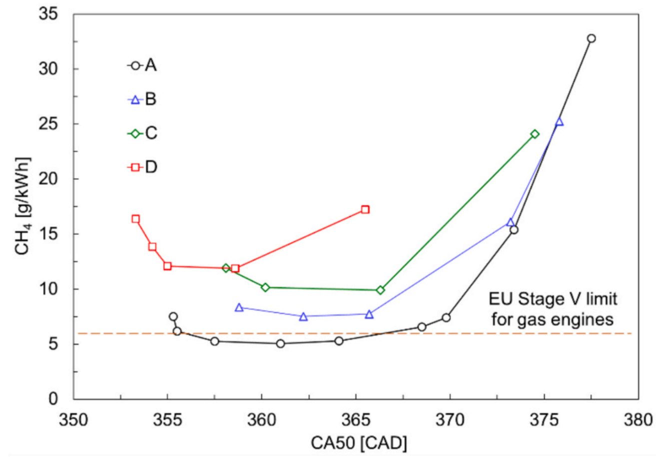

Fig. 12. Indicated specific emission of methane versus CA50.

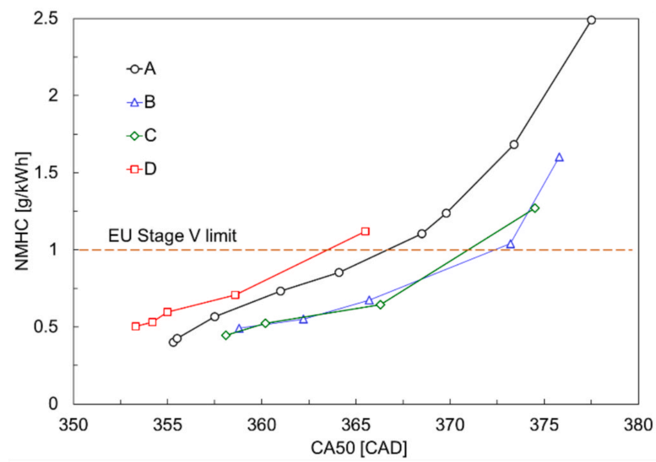

Fig. 13. Indicated specific emission of NMHC versus CA50.

NMHC emissions (Fig. 13) generally align with earlier findings: stronger swirl intensifies mixing in the squish and crevice regions, increasing the amount of charge trapped in locally over-diluted, low-temperature zones where partial oxidation pathways dominate. The behaviour observed for cases A and D further highlights the influence of flow structures other than swirl – particularly local turbulences – in mediating the transport of reactive intermediates between the squish region and the piston bowl, thereby shaping the late-oxidation chemistry. When interpreted together with the combustion indicator trends, this appears to be the most plausible explanation for the weaker correlation between NMHC emissions and CH4 and CO in case A. It should be noted, however, that the formation of NMHC originating from the liquid-fuel fraction is inherently complex, and this interpretation does not fully exclude the contribution of additional effects, such as weaker near-wall charge renewal or localised wall impingement linked to the very early injections characteristic of case A. Nevertheless, these mechanisms appear to play a secondary role within the operating range considered.

Fig. 14 depicts the evolution of CO emissions. Like the CH_4 trends, CO formation shows a strong sensitivity to combustion phasing, with emissions increasing sharply when combustion is delayed beyond

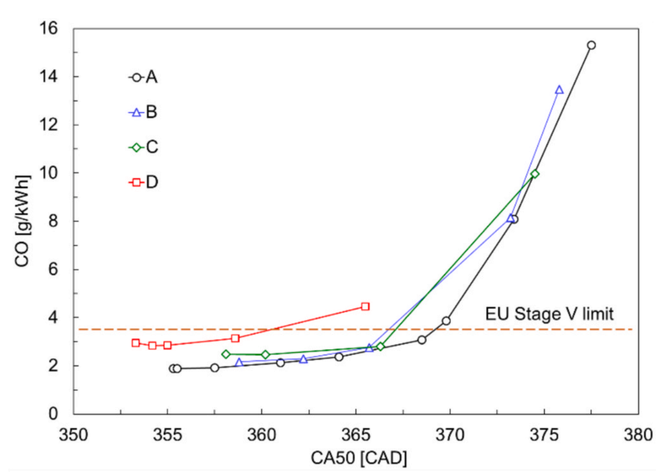

Fig. 14. Indicated specific emission of CO versus CA50.

approximately 370 CAD. In early phasing conditions (CA50 < 365 CAD), the neutral and low-swirl configurations yield the lowest CO levels, reflecting more complete oxidation of intermediates in a well-mixed and sufficiently hot environment.

Case D (SR = 4.5) consistently exhibits the highest CO emissions across the entire CA50 sweep. This is attributed to stronger swirl-induced mixing in the squish region, leading to excessive dilution of the HRF and lower local equivalence ratios. Combined with intensified heat transfer to the combustion chamber surfaces – an inherent consequence of high swirl – the local temperatures during the late oxidation phase are too low to convert CO to CO2 fully.

Fig. 15 shows that NO_X emissions clearly correlate with CA50, while remaining unaffected by SR. However, one outlier – case D; CA50 = 356.5 CAD – shows significantly lower NO_X emissions. This anomaly is attributed to two overlapping effects: enhanced charge homogenisation (as evident in Fig. 4) and substantial cooling due to a high SR. A comparison of case D and case A (CA50 = 364 CAD), both featuring the same start of injection (SOI = 42 CAD bTDC) and similar levels of HRF homogenisation, highlights the dominant role of swirl in reducing NO_X. In contrast, neighbouring cases B and C – despite having later injection timings (38 CAD bTDC) and less homogenised mixtures – align with the main NO_X trend line. This proves that HRF stratification (at ignition onset) does not determine NO_X formation in RCCI combustion, as suggested by Mohammadnejad et al. [21]. Instead, overall temperature conditions and intensive mixing during combustion effectively prevent NO_X formation.

Fig. 16 shows PM emissions for all investigated conditions. Overall, PM mass remains at very low levels typical of RCCI (approximately 1 mg/kWh), with minimal emissions observed for cases A and B. A comparison of Figs. 15 and 16 shows that the typical diesel combustion NO_X/PM trade-off does not exist in the explored RCCI regime. Early combustion, associated with shorter ID, induces the formation of PM. At the same ID of 25 CAD, the higher the homogenisation, the higher the PM emissions, which is counterintuitive. The differences between the swirl cases disappear for CA50 above 365 CAD, as the in-cylinder temperature associated with delayed combustion is below the threshold of soot formation.

Fig. 17's PN_{23} trends (PN emissions calculated for particles with diameters greater than 23 nm) reveal a non-monotonic characteristic. At early combustion, for CA50 < 365, the trend is the same as for PM, but a delay of CA50 beyond 365 CAD results in an increase in PN. Premixed conditions produce more fine particles, especially sub-23 nm particles, not shown in Fig. 17. The PN_{10} emission at CA50 of 375 CAD is around 4 $\times$ 10^{13} for cases A, B and C.

It should be noted that particles in nucleation mode with diameters lower than 50 nm consist of a high fraction of semi-volatile material.

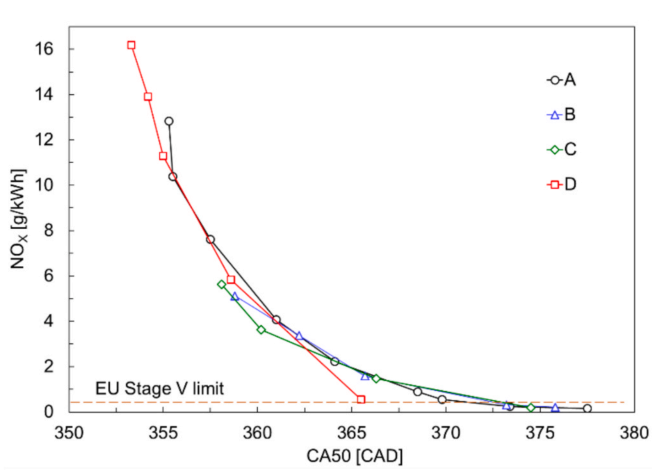

Fig. 15. Indicated specific emissions of NO_X versus CA50.

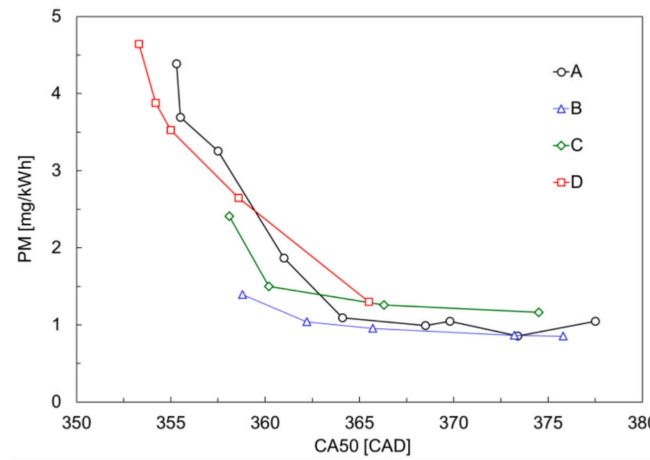

Fig. 16. Indicated specific emissions of PM versus CA50.

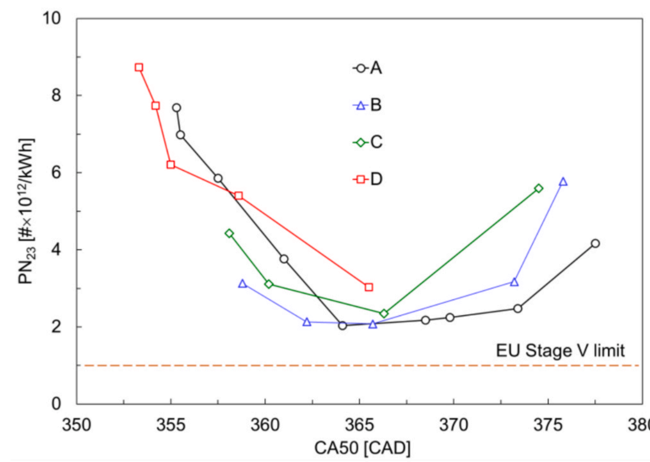

Fig. 17. Indicated specific emissions of PN_{23} versus CA50.

Due to this aerosol composition, the electrical mobility measurement principle used in this research typically overestimates PN by 25% compared to normative condensation particle counting [31]. For the same reason, PN can be reduced using an oxidation catalyst. Garcia et al. [32] demonstrated that at a moderate exhaust temperature, an oxidation catalyst can reduce particle concentrations smaller than 30 nm by more than an order of magnitude, thereby reducing minimal emissions, as shown in Fig. 17, to 1.6 x 10^{12} #/kWh. Additionally, fine particles are efficiently removed by diesel particulate filters, with reported filtration efficiencies of up to 95%. This is primarily due to Brownian motion-driven diffusion, which promotes particle deposition on the filter structure [33].

3.6. Optimising RCCI for different SR configurations

The overall effect of SR and SOI on RCCI performance is presented in the form of an overlimit function according to Eq. (2), and the resulting values are depicted in Fig. 18.

It is immediately apparent in Fig. 18 that optimal RCCI combustion can be achieved with CA50 between 365 and 370 CAD. Although high thermal efficiency can be maintained over a wider range, the applicable CA50 window is effectively constrained by emission limits. For more advanced combustion phasing, NO_X emissions become the primary limiting factor. Conversely, for retarded CA50 values, CH_4 emissions and increased combustion variability impose the main constraints. Interestingly, this CA50 range also corresponds to the lowest PN emissions – a

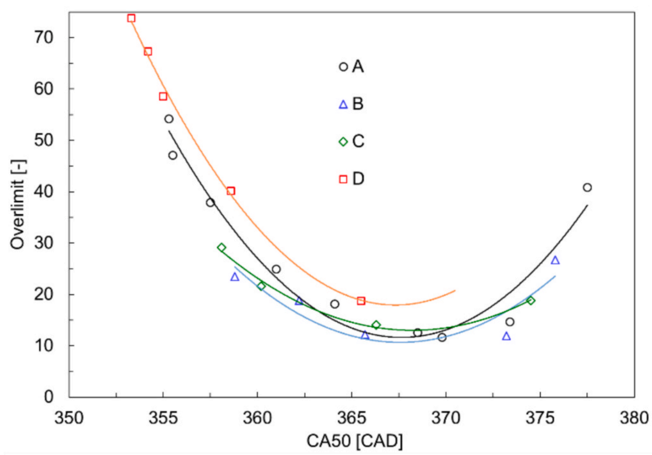

Fig. 18. Overlimit function values versus CA50.

factor that is often overlooked in RCCI research.

This confirms that CA50 is a major factor determining efficiency, combustion stability and emissions. Other factors, like ID, have secondary effects. At moderate levels, SRs do not significantly affect the overlimit, whereas high SRs introduce a strong trade-off between NO_X emissions and combustion efficiency. Increased emissions of CH4, CO and NMHC manifest the latter.

Note that the main outcomes do not qualitatively change with sensitivity to the selection of the weighting factor. In particular, for the arbitrarily selected double weighting of CH_4 emissions rationalised in Section 2.6, variations of the weighting factor within the range of 1.2 to 2 do not alter the relative trends among the investigated SR configurations. Specifically, the position of the minimum of the over-limit function with respect to SOI remains unchanged across all tested cases. This confirms that the observed optima and comparative behaviour are robust with respect to the assumed CH_4 weighting.

4. Conclusions

This study experimentally evaluated the coupled effects of SR and diesel SOI on diesel-natural gas RCCI combustion. The findings substantiate the central hypothesis that an optimal SR arises from the balance between enhancing reactivity stratification and inducing over-homogenisation or excessive wall cooling, with this optimum being strongly conditioned by diesel injection timing and combustion-chamber geometry. At the same time, the results extend beyond the original hypothesis by demonstrating that the relevance of in-cylinder flow behaviour is more complex than the swirl effect alone and cannot be interpreted in isolation. The main outcomes are as follows:

1. Flow-field effects are fundamentally coupled with spray–geometry interaction. Combustion under the present engine configuration consistently initiates in the hotter, centrally located bowl region, indicating that the influence of swirl or tumble cannot be evaluated independently of early diesel spray targeting and subsequent bowl–squish flow redistribution.
2. Ignition timing is largely swirl-insensitive, verifying bowl-governed auto-ignition. Configurations with a distinct, single-port-induced turbulence (cases A and D) ignited approximately 5 CAD earlier than cases with both ports open. This highlights that ignition is primarily governed by spray-induced reactivity stratification and secondarily by local turbulences, rather than radial, transport.
3. Local turbulence-driven redistribution extends the RCCI ignitability window. Weak-turbulence configurations experienced abrupt misfire once injection was advanced to the point where the diesel spray missed the bowl and targeted the squish region (SOI earlier than 40 CAD bTDC). In contrast, the strong-turbulent-energy neutral-port-only configuration maintained stable combustion for SOIs as early as 47 CAD bTDC.
4. Swirl effects become statistically significant as combustion reaches the squish region. At an ignition onset of 354 CAD, CA50 occurred at 363.2, 360.2 and 358.6 CAD for SR = 1.7, 2.9 and 4.5, respectively. Peak heat-release rate increased by > 20% from the lowest to highest SR, confirming a monotonic SR influence on combustion development.
5. Flow-field influence decays rapidly after top dead centre. For combustion onset values greater than 365 CAD, peak HRR and combustion duration converged across all SRs, indicating that late-cycle combustion is dominated by thermal rather than flow phenomena.
6. High swirl does not yield higher efficiency. Despite faster combustion, SR = 4.5 consistently exhibited combustion efficiencies 2–4 percentage points lower and indicated thermal efficiencies lower than those of lower SR configurations. The efficiency penalty is attributable to swirl-enhanced wall cooling and reduced local stratification.
7. Emission behaviour is consistent with the observed combustion phenomenology.
   - CH_4: Increased monotonically with SR, due to enhanced dilution and reduced late-cycle temperatures.
   - CO: Highest for SR = 4.5, explained by over-mixed, over-cooled boundary-layer regions.
   - NMHC: Followed swirl intensity except for the neutral-port-only case, where strong turbulences facilitated bowl–squish exchange, decoupling NMHC behaviour from CH_4 and CO.
   - NO_X: Determined solely by CA50 and temperature, which was further reduced at high SR by heat transfer.
   - PM: Overall, mass-based emissions are low and show little sensitivity to SR when sufficient mixing time is ensured. In contrast, particle number emissions display a non-monotonic dependence, reaching a minimum at the operating condition corresponding to optimal gaseous emissions. Nevertheless, particle number emissions remain high, exceeding the EU Stage V regulatory limit by a factor of two.
8. The neutral-port-only configuration provided the most balanced performance. It achieved the lowest combined hydrocarbon and CO emissions – within EU Stage V-equivalent engine-out limits – and the highest indicated thermal efficiency of 43.8%. This confirms that a favourable balance between swirl, tumble and local turbulences yields the broadest SOI calibration window and the most robust RCCI operation.

The quantification of the effects described above remains specific to the research object, but the mechanisms and trends outlined in the conclusions are directly transferable to other engine geometries and fuels, within the boundaries of RCCI and its characteristic reactivity and thermal stratification patterns. The findings thus support knowledge-driven development of next-generation engines, particularly in the widely established off-road sector, where such optimisation may enable compliance with stringent emission limits without reliance on exhaust aftertreatment.

CRediT authorship contribution statement

Jacek Hunicz: Writing – review & editing, Writing – original draft, Validation, Methodology, Investigation, Funding acquisition, Formal analysis, Data curation, Conceptualization. **Liping Yang:** Writing – review & editing, Validation, Supervision, Resources, Project administration, Methodology, Funding acquisition, Formal analysis, Data curation. **Shuaizhuang Ji:** Writing – original draft, Visualization, Software, Formal analysis, Data curation. **Maciej Mikulski:** Writing – review & editing, Writing – original draft, Validation, Supervision, Resources, Investigation, Funding acquisition, Conceptualization.

Declaration of competing interest

The authors declare the following financial interests/personal relationships which may be considered as potential competing interests: [Maciej Mikulski reports financial support was provided by Business Finland. Jacek Hunicz reports financial support was provided by Business Finland. Jacek Hunicz reports financial support was provided by Chinese Ministry of Science and Technology. Liping Yang reports financial support was provided by National Natural Science Foundation of China. Jacek Hunicz reports financial support was provided by Republic of Poland Ministry of Science and Higher Education. If there are other authors, they declare that they have no known competing financial interests or personal relationships that could have appeared to influence the work reported in this paper.].

Acknowledgements

Jacek Hunicz and Liping Yang gratefully acknowledge the Chinese Ministry of Science and Technology for supporting this research through the National Foreign Experts Program (grant No. G2023180006L) and National Natural Science Foundation of China (grant No. 52171298).

The experimental research was supported by the commissioned task Via Carpatia – Universities of Technology Network (grant No. MEiN/2022/DPI/2575).

Maciej Mikulski and Jacek Hunicz acknowledge the Flexible Clean Propulsion Technologies project with financial support from Business Finland (ref. 1310/31/2023).

Appendix A. Supplementary data

Supplementary data to this article can be found online at https://doi.org/10.1016/j.enconman.2026.121743.

Data availability

Data will be made available on request.

References

[1] Kokjohn SL, Hanson RM, Splitter DA, Reitz RD. Experiments and modeling of dual-fuel HCCI and PCCI combustion using in-cylinder fuel blending. SAE Int J Engines 2010;2:24–39. https://doi.org/10.4271/2009-01-2647.
[2] Yang L, Ji S, Niu W, Zare A, Hunicz J, Brown RJ. Effect of split injection strategy of diesel fuel on multi-stage heat release and performance of a RCCI engine fueled with diesel and natural gas. Fuel 2024;362. https://doi.org/10.1016/j.fuel.2024.130930.
[3] Paykani A, Garcia A, Shahbakhti M, Rahnama P, Reitz RD. Reactivity controlled compression ignition engine: pathways towards commercial viability. Appl Energy 2021;282. https://doi.org/10.1016/j.apenergy.2020.116174.
[4] Reitz RD, Duraisamy G. Review of high efficiency and clean reactivity controlled compression ignition (RCCI) combustion in internal combustion engines. Prog Energy Combust Sci 2015;46:12–71. https://doi.org/10.1016/j.pecs.2014.05.003.
[5] Benajes J, García A, Monsalve-Serrano J, Boronat V. Achieving clean and efficient engine operation up to full load by combining optimized RCCI and dual-fuel diesel-gasoline combustion strategies. Energy Convers Manag 2017. https://doi.org/10.1016/j.enconman.2017.01.010.
[6] Duan H, Jia M, Li Y, Wang T. A comparative study on the performance of partially premixed combustion (PPC), reactivity-controlled compression ignition (RCCI), and RCCI with reverse reactivity stratification (R-RCCI) fueled with gasoline and polyoxymethylene dimethyl ethers (PODEn). Fuel 2021;298; doi: 10.1016/j.fuel.2021.120838.
[7] Mohammed Elbanna A, Xiaobei C, Can Y, Elkelawy M, Alm-Eldin Bastawissi H, Panchal H. Fuel reactivity controlled compression ignition engine and potential strategies to extend the engine operating range: a comprehensive review. Energy Convers Manag X 2022;13. https://doi.org/10.1016/j.ecmx.2021.100133.
[8] Chaudhari VD, Deshmukh D. Fuel flexibility study of various fuels with charge dilution and high compression ratio for medium-load operating RCCI engine. Fuel 2022;310. https://doi.org/10.1016/j.fuel.2021.122163.
[9] Kakoee A, Hunicz J, Mikulski M. Integrated 1D simulation of aftertreatment system and chemistry-based multizone RCCI combustion for optimal performance with methane oxidation catalyst. J Mar Sci Eng 2024;12. https://doi.org/10.3390/jmse12040594.
[10] Hunicz J, Yang L, Rybak A, Ji S, Gęca MS, Mikulski M. Comparison of diesel and hydrotreated vegetable oil as the high-reactivity fuel in reactivity-controlled compression ignition. Energy Convers Manag 2025;323:119264. https://doi.org/10.1016/j.enconman.2024.119264.
[11] Agarwal AK, Singh AP, García A, Monsalve-Serrano J. Challenges and opportunities for application of reactivity-controlled compression ignition combustion in commercially viable transport engines. Prog Energy Combust Sci 2022;93. https://doi.org/10.1016/j.pecs.2022.101028.
[12] Szamrej G, Karczewski M, Chojnowski J. A review of technical solutions for rcci engines. Combust Engines 2022;189:36–46. https://doi.org/10.19206/CE-142551.
[13] Dempsey AB, Ryan Walker N, Reitz R. Effect of piston bowl geometry on dual fuel reactivity controlled compression ignition (RCCI) in a light-duty engine operated with gasoline/diesel and methanol/diesel. SAE Int J Engines 2013;6:78–100. https://doi.org/10.4271/2013-01-0264.
[14] Oh S, Oh J, Jang HJ, Lee S, Lee S, Kim C, et al. Effects of piston shape and nozzle specifications on part-load operation of natural gas–diesel dual-fuel RCCI engine and its application to high load extension. Fuel 2022;328. https://doi.org/10.1016/j.fuel.2022.125361.
[15] Feng Y, Sun K, Li Y, Bai H, Shi L, Lu Z, et al. The critical role of swirl in high-specific-output diesel engines. Fuel 2023;341. https://doi.org/10.1016/j.fuel.2023.127636.
[16] Cui Z, Ye M, Zhang H, Tian J, Zhang X, Yin S. Optical study on the combustion process of diesel/natural gas dual fuel engine with in-cylinder swirl. Fuel 2025;392. https://doi.org/10.1016/j.fuel.2025.134915.
[17] Curran S, Prikhodko V, Cho K, Sluder C, Parks J, Wagner R, et al. In-cylinder fuel blending of gasoline/diesel for improved efficiency and lowest possible emissions on a multi-cylinder light-duty diesel engine. SAE Tech Pap 2010. https://doi.org/10.4271/2010-01-2206.
[18] Kokjohn S, Hanson R, Splitter D, Kaddatz J, Reitz R. Fuel reactivity controlled compression ignition (RCCI) combustion in light- and heavy-duty engines. SAE Int J Engines 2011;4:360–74. https://doi.org/10.4271/2011-01-0357.
[19] Yousefi A, Guo H, Birouk M. Effect of swirl ratio on NG/diesel dual-fuel combustion at low to high engine load conditions. Appl Energy 2018;229:375–88. https://doi.org/10.1016/j.apenergy.2018.08.017.
[20] Dadsetan M, Chitsaz I, Amani E. A study of swirl ratio effects on the NOx formation and mixture stratification in an RCCI engine. Energy 2019;182:1100–14. https://doi.org/10.1016/j.energy.2019.06.109.
[21] Mohammadnejad S, Amani E, Hosseini R, Chitsaz I, Kamali A. Effects of the swirl ratio and spray angle on the mixture stratification in a diesel–NG RCCI engine. J Brazilian Soc Mech Sci Eng 2019;41. https://doi.org/10.1007/s40430-019-1736-5.
[22] Yazdani K, Amani E, Naderan H. Multi-objective optimizations of the boot injection strategy for reactivity controlled compression ignition engines. Int J Engine Res 2019;20:889–910. https://doi.org/10.1177/1468087418795599.
[23] Zhou W, Gao J, Zhang Z, Wang H. Optimization of combustion strategies for heavy-duty ammonia/diesel dual-fuel engine under different combustion mode. Int J Hydrogen Energy 2025;184. https://doi.org/10.1016/j.ijhydene.2025.151798.
[24] Hohenberg GF. Advanced approaches for heat transfer calculations. SAE Tech. Pap., SAE International; 1979, p. 790825.; doi: 10.4271/790825.
[25] Ovaska T, Spoof-Tuomi K, Niemi S, Valkjärvi P, Maunula T, Mikulski M, et al. Effect of late diesel injection on close-coupled SCR + ASC during DPF regeneration period. Fuel 2025;381. https://doi.org/10.1016/j.fuel.2024.133406.
[26] Kim J, Soleimani A, Nousiainen P, Axelsson M, Mikulski M. Variable valve actuation (VVA) for next-generation marine and off-road engines: a comprehensive review for meeting future emissions legislation. Appl Energy 2026;406. https://doi.org/10.1016/j.apenergy.2025.127133.
[27] Lehtoranta K, Koponen P, Vesala H, Kallinen K, Maunula T. Performance and regeneration of methane oxidation catalyst for LNG ships. J Mar Sci Eng 2021;9:1–12. https://doi.org/10.3390/jmse9020111.
[28] Lu T, Lu Z, Gao Y, Shi L, Wang H, Wang T. Investigation on suitable swirl ratio and spray angle of a large-bore marine diesel engine using genetic algorithm. Fuel 2023;345. https://doi.org/10.1016/j.fuel.2023.128187.
[29] Vasudev A, Kakoee A, Axelsson M, Almani HM, Hyvönen J, Mikulski M. Advancing autonomy of chemical kinetics based multizone models for reactivity controlled compression ignition engines. Energy Convers Manag 2024;312. https://doi.org/10.1016/j.enconman.2024.118562.
[30] Yang L, Ji S, Hunicz J, Wang R, Zare A, Su Y, et al. Analysis of multi-mode combustion and performance in a marine diesel/natural gas dual-fuel engine based on an irreversible equivalent combustion cycle theory. Energy 2025;326. https://doi.org/10.1016/j.energy.2025.136248.
[31] Giechaskiel B, Melas A. Comparison of Particle Sizers and Counters with Soot-like, Salt, and Silver Particles. Atmosphere (Basel) 2022;13. https://doi.org/10.3390/atmos13101675.
[32] García A, Monsalve-Serrano J, Villalta D, Fogué-Robles Á. Detailed analysis of particulate emissions of a multi-cylinder dual-mode dual-fuel engine operating with diesel and gasoline. Fuel 2022;330. https://doi.org/10.1016/j.fuel.2022.125578.
[33] Rossomando B, Meloni E, de Falco G, Sirignano M, Arsie I, Palma V. Experimental characterization of ultrafine particle emissions from a light-duty diesel engine equipped with a standard DPF. Proc Combust Inst 2021;38:5695–702. https://doi.org/10.1016/j.proci.2020.09.011.